Supplementary Information

Cation-regulated MnO_2 Reduction Reaction Enabling Long-term Stable Zinc-Manganese Flow Batteries with High Energy Density

Yiqiao Wang[1], Hu Hong[1], Zhiquan Wei[1], Dedi Li[1], Xinru Yang[1], Jiaxiong Zhu[1], Pei Li[1], Shengnan Wang[1] and Chunyi Zhi[1]*

[1]Department of Materials Science and Engineering, City University of Hong Kong, 83 Tat Chee Avenue, Kowloon, Hong Kong 999077, China

*Corresponding Author

E-mail: cy.zhi@cityu.edu.hk (C. Zhi)

Table of Contents:

Experimental section

Materials

All reagents in this work are purchased analytically pure and without further purification. Manganese chloride ($MnCl_2$) (Alfa Aesar, 99%), Magnesium chloride hexahydrate ($MgCl_2 \cdot H_2O$) (Sigma-Aldrich, 99%), Zinc acetate ($Zn(Ac)_2$) (Aladdin, 99%), Acetic acid (HAc) (Aladdin, AR) and Hydrochloric acid (HCl) (RCI Labscan, AR) were used for preparing electrolytes. All electrolytes were prepared with deionized (DI) water. Potassium hydroxide (KOH) (Aladdin, 99 %), Sulfuric acid (H_2SO_4) (RCI Labscan, AR), Nafion membrane (N117, Dupont) was purchased from SCI Materials Hub. Hydrogen peroxide (H_2O_2) (Sigma-Aldrich, 30 wt% in H_2O) was purchased for the pre-treatment of the Nafion membrane. Carbon felt (CF) purchased from Liaoyang J-Carbon Materials Co., Ltd. (China) was used as received.

Preparation of proton exchange membrane

The received Nafion N117 membranes were pre-treated with the following steps before use. First, the membrane was soaked in 5 wt% H_2O_2 solution at 80 ℃ for 1 hour, followed by flushing with DI water to remove excess H_2O_2. Then, the Nafion membrane was soaked in 0.5 M H_2SO_4 at 80 ℃ for 1 hour and rinsed with DI water until the pH reached 7. Finally, the membrane was rinsed with DI water and stored in DI water.

Materials characterization

Fourier transform infrared spectrometer (FT-IR, PerkinElmer) and Raman spectrometer (WITec RAMAN alpha 300R) were used to analyze electrolyte composition and molecular interaction. X-Ray Diffraction (XRD, Rigaku X-ray Diffractometer SmartLab 9 kW), Scanning Electron Microscopy (SEM, Quattro S, Thermo Fisher Scientific) equipped with an energy-dispersive X-ray spectroscopy (EDS), Transmission electron microscopy (FEI Tecnai G2F 20), Raman spectroscopy and X-ray photoelectron spectroscopy (XPS, Thermal Fisher Scientific Escalab-Xi+) were employed to identify the product species and structure of cathode being discharged and charged.

Electrochemical characterization

LSV and CV measurements were carried out on the single-channel electrochemical workstation (CHI-760E) in a conventional single compartment three-electrode cell configuration at room temperature

(25 ℃). Ag/AgCl electrode in saturated KCl was employed as a reference electrode (RE), a graphite rod and a platinum plate was served as the working (WE) and counter electrode (CE), respectively. The potential of WE was referenced to a standard hydrogen electrode (SHE) using this equation.

$$E_{SHE}=E_{Ag/AgCl}-0.22\ V$$

The LSV experiment was coupled with a gas chromatograph (GC), in which the Argon gas was employed as carrier gas.

The Tafel plot is obtained by plotting the overpotential against the logarithmic current density as the following equation.

$$\eta=b*log(j)+a$$

Where η is the overpotential $E-E_0$, b refers to the tafel slope.

The EIS spectra were collected in the ultra low temperature chamber (ESPEC MC-812) by CHI-760E, the frequency range variated from 10^6 Hz to 10^{-1} Hz for the two-electrode potentiostatic Zn-Mn batteries. The corresponding reaction resistance R_{ct} at different temperatures was obtained by fitting the equivalent circuit model of EIS. The apparent activation energy (E_a) of the reaction at 1.6 V can be given according to the Arrhenius equation.

$$k=A*exp(-E_a/RT)$$

Zn-Mn flow battery assembly

The zinc-manganese flow battery (AZIFB) was assembled by sandwiching a membrane between two CF electrodes clamped by two graphite plates. The stainless-steel end plates were used to secure the battery. The active area of the electrode is 2×2 cm^2 with a thickness of 3 mm. The pre-treated Nafion membrane was used to separate the catholyte and anolyte. The anolyte contained 3 M $ZnCl_2$, 1 M $Zn(Ac)_2$ and 1M HAc . The 1 M $MnCl_2$ and 0.2 M HCl with/without 4 M $MgCl_2$ were used as the Mn-H/Mn-Mg-H catholyte, respectively. Both the capacity of the cathode and anode were contributed by the active ions in the electrolytes, with the CFs acting as current collectors and no additional zinc or manganese sources to supplement them. A peristaltic pump from Chuang Rui Co. Ltd. was served to power the electrolyte flow through the electrodes. All the battery performance tests were conducted by LAND CT3001A multi-channel battery system.

Inductively Coupled Plasma Mass Spectrometry (ICP-MS) Measurements

The quantitative elemental analysis of the discharge products was performed by the ICP-MS (Agilent 720ES). The discharged batteries were disassembled and the carbon felt from the cathode side was washed to remove residual electrolytes. After being cleaned and dried overnight, the carbon felt was ground and digested with concentrated hydrochloric acid. The suspension was filtered to remove residual carbon fibers to obtain the sample dispersion containing Mg^{2+} and Mn^{2+}.

Gas Chromatography Measurements

The oxygen evolution amounts were measured by an online gas chromatograph (Ruimin GC 2060) with a packed HayeSep D column and a thermal conductivity detector (TCD) for O_2 quantification. Calibration gas mixtures (Linde) were employed for gas quantification. The continuous flow of Argon gas through the electrochemical cell carried volatile reaction products from the cell into the sampling loops of the GC.

Molecular dynamics (MD) simulations

MD simulations were performed using the Forcite module with the COMPASSIII forcefield[1]. For electrolyte structure determination, the simulation boxes containing 40 $MnCl_2$ and 8 HCl or 160 $MgCl_2$, 40 $MnCl_2$ and 8 HCl with 2000 H_2O molecules corresponding to Mn-H and Mn-Mg-H, respectively, were established by amorphous cell module. Subsequently, all mixture systems were equilibrated by constant-pressure and constant-temperature (NPT) MD simulations for 1 ns at 303 K, after which canonical ensemble (NVT) MD simulations were used for 1 ns. The Ewald method[2] and atom-based cutoff method (i.e., a radius of 12.5 Å) were applied to conduct electrostatic and van der Waals (vdW) interactions, respectively.

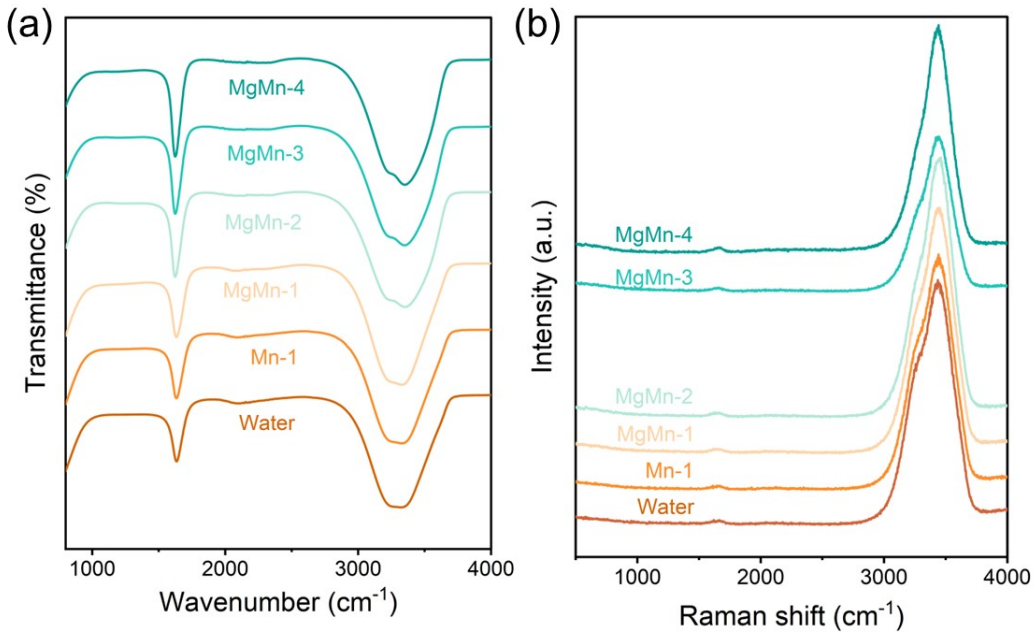

Figure S1 Full profile of FT-IR and Raman spectra of the Mn-H and Mn-Mg-H with different concentrations.

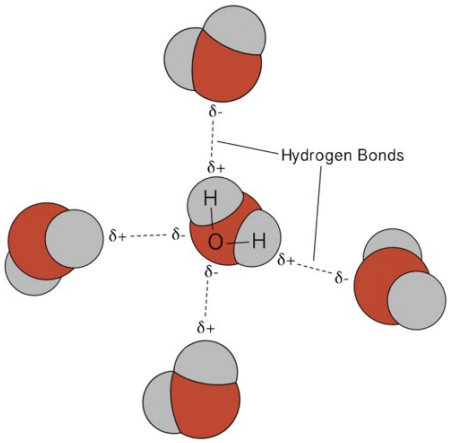

Figure S2 Schematic of H-bonds between water molecules.

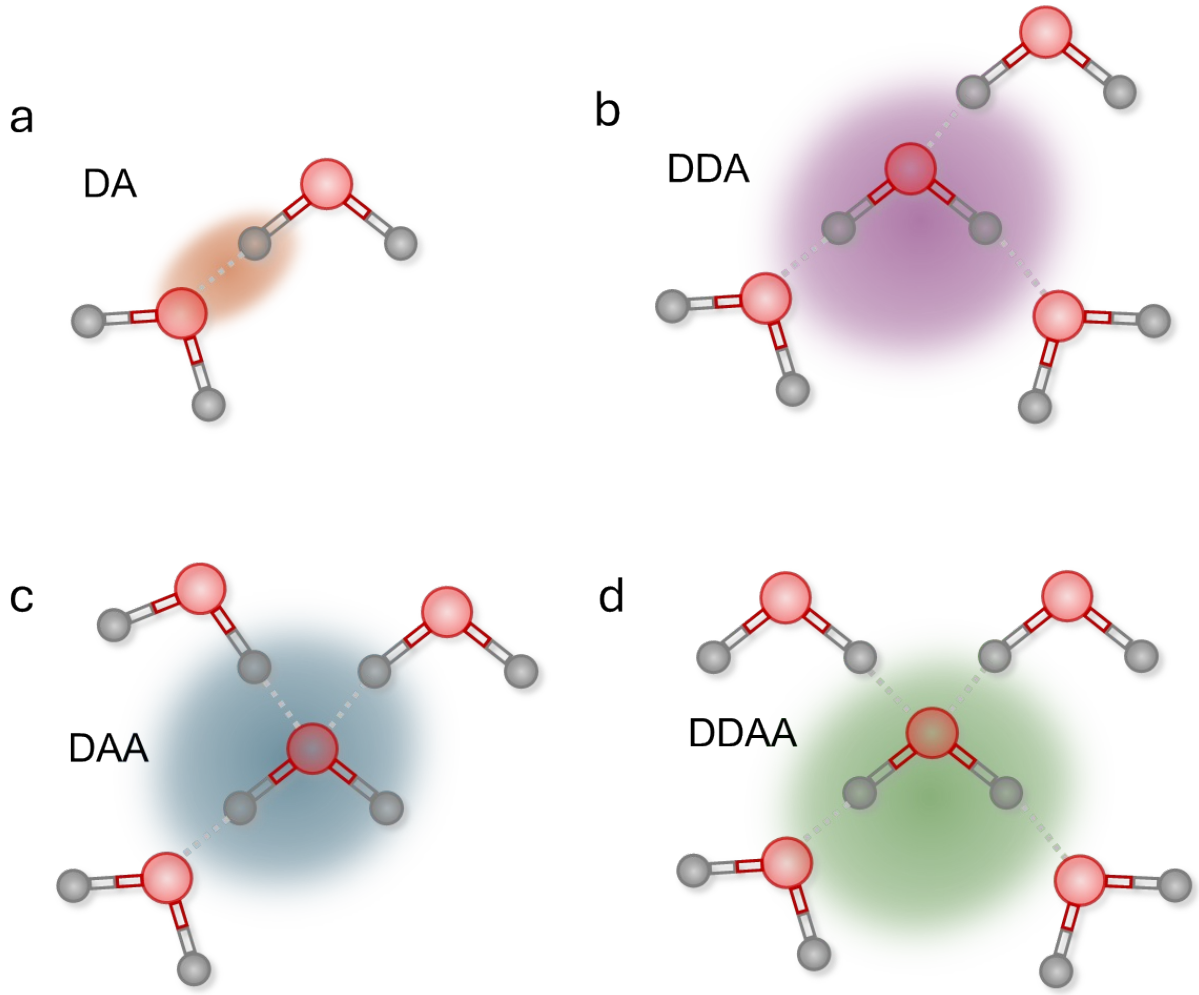

Figure S3 Schematic of water molecules with (a) DA, (b) DDA, (c) DAA and (d) DDAA type H-bonds.

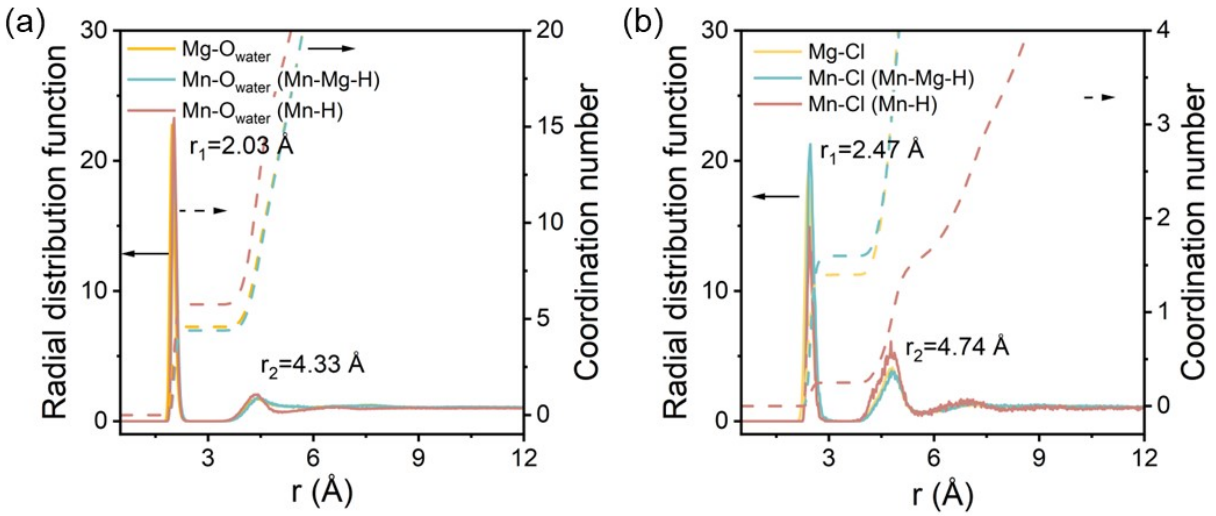

Figure S4 Radial distribution functions of Mn-H and Mn-Mg-H show the first and second radii of the solvation shell.

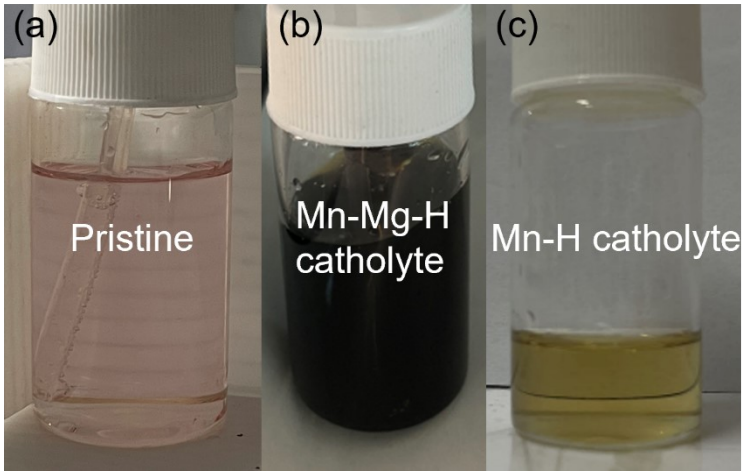

Figure S5 Digital image of the catholyte during charging.

(a) Mn-Mg-H based catholyte (a) before and (b) after positive scanning. (c) Mn-H based catholyte after charging.

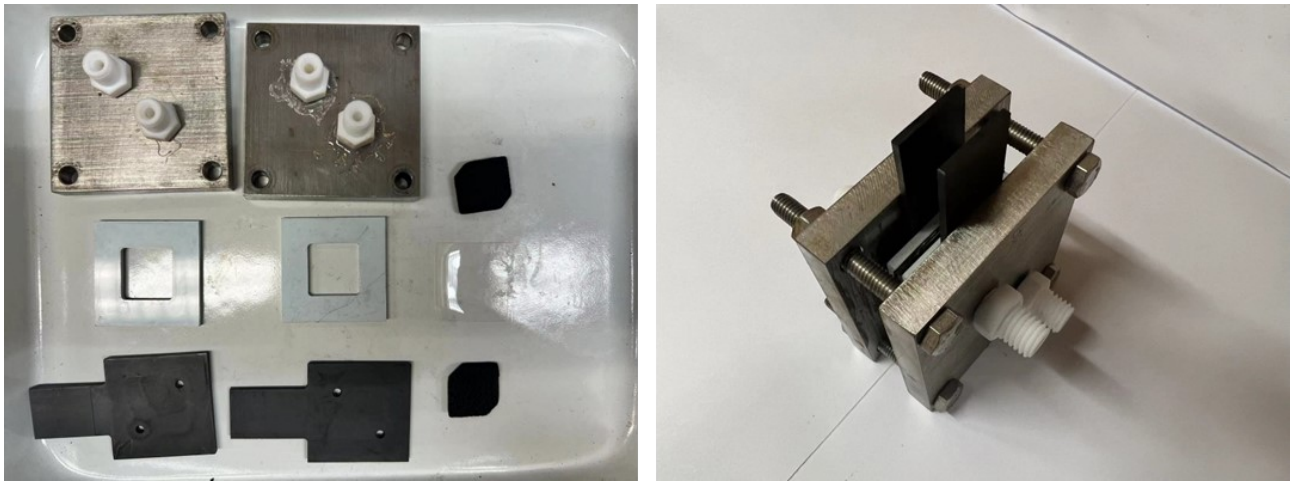

Figure S6 Digital image of the Zn-Mn flow battery configuration.

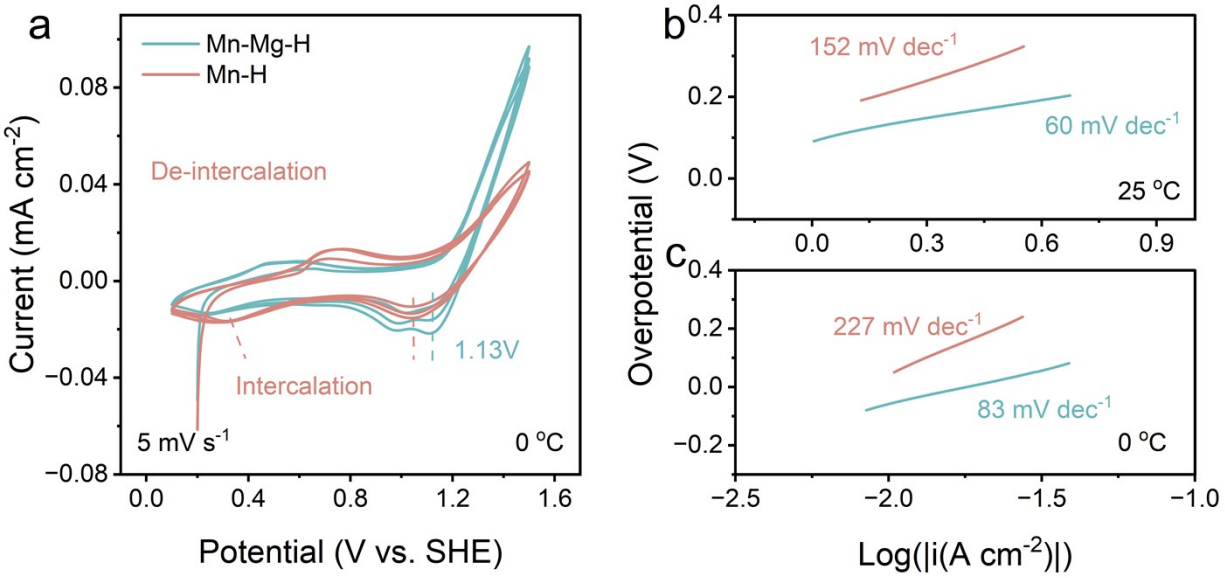

Figure S7 Cyclic voltammetry of MnO_2 conversion reaction in Mn-H and Mn-Mg-H system at (a) 0 ℃, respectively. The corresponding Tafel plots in (b) 25 ℃ and (c) 0 ℃ obtained from the initial cycle of CV curves.

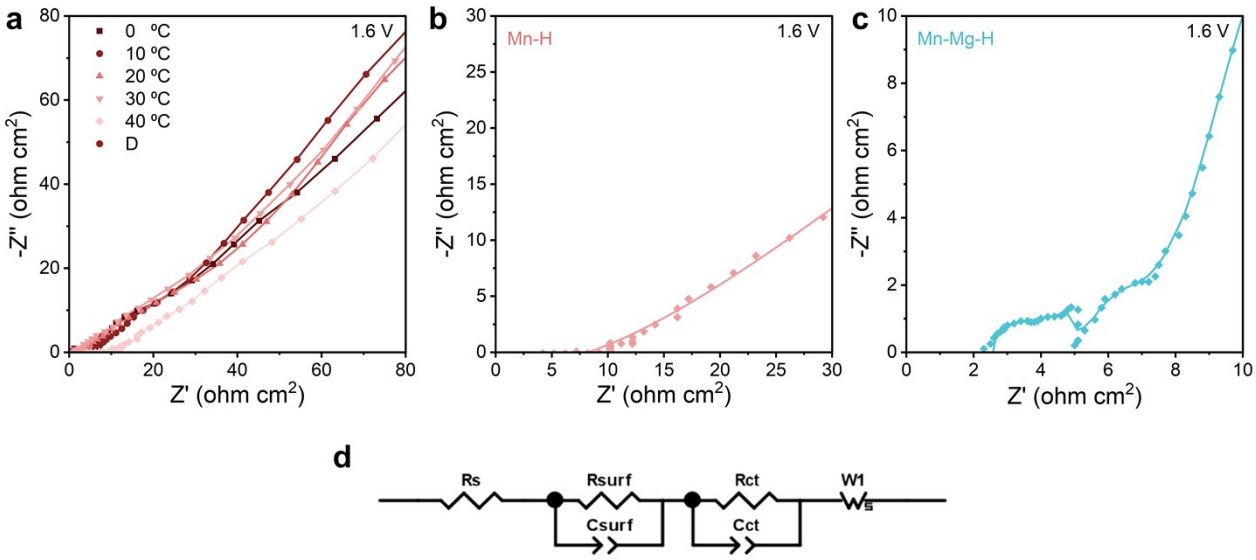

1

2 Figure S8 EIS spectra and equivalent circuit of Mn-H and Mn-Mg-H-based Zn-Mn FBs

3 (a) Nyquist plots of Mn-H-based Zn-Mn FBs at 0-40 ℃. Nyquist plot of (b) Mn-H and (c) Mn-Mg-H based batteries

4 at high frequencies of EIS at 40 ℃. (d) Schematic of the equivalent circuit. The inset equivalent circuit is used to

5 simulate the resistances, where R_s is the ohmic resistance, R_{surf} and C_{surf} are the charge-transfer resistance and double-

6 layer capacitance at anode/electrolyte interphase, R_{ct} and C_{ct} are the charge-transfer resistance and double-layer

7 capacitance at cathode/electrolyte interphase, and W_1 is the Warburg impedance.

8

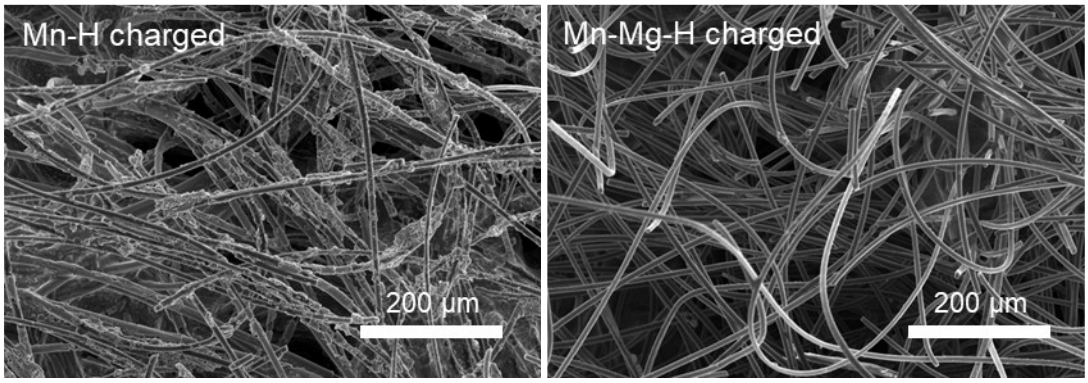

Figure S9 SEM images of the charged cathode.

(a) SEM image of the Mn-H cathode. (b) SEM image of the Mn-Mg-H cathode.

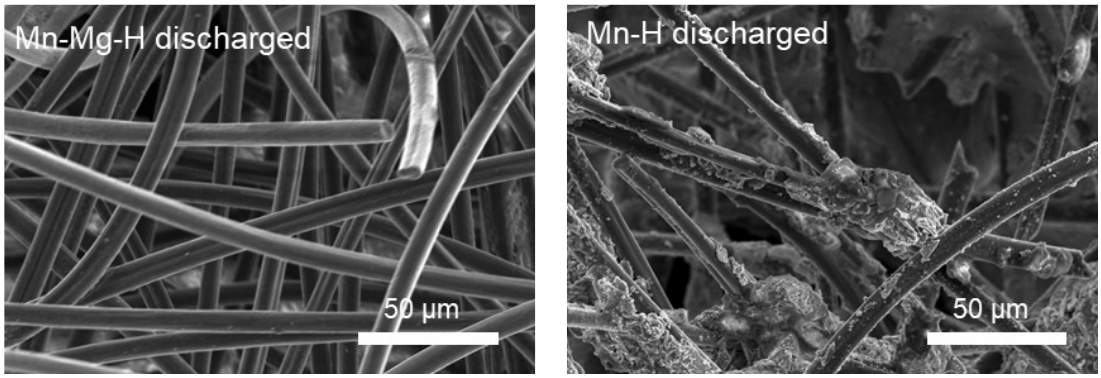

Figure S10. SEM images of the discharged cathode.

(a) SEM image of the Mn-Mg-H cathode. (b) SEM image of the Mn-H cathode.

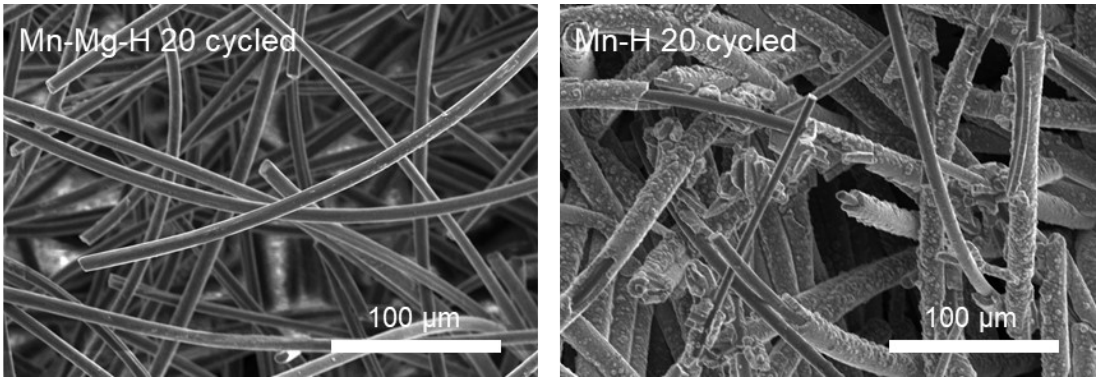

Figure S11. SEM images of the cathode after 20 cycles.

(a) SEM image of the Mn-Mg-H cathode. (b) SEM image of the Mn-H cathode.

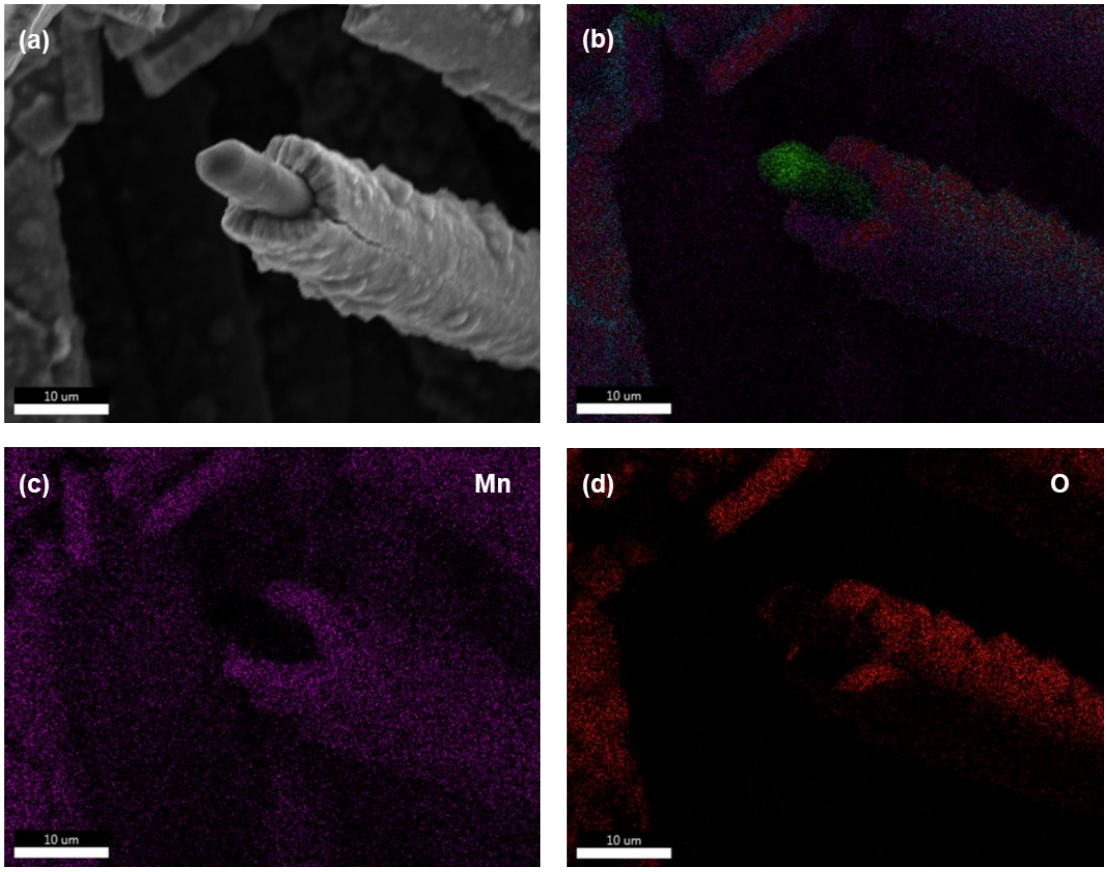

Figure S12. EDS mapping of the cathode in Mn-H electrolyte.

(a) SEM image of the charged Mn-H cathode. (b) Overlapped image, (c) Mn and (d) O element of EDS mapping.

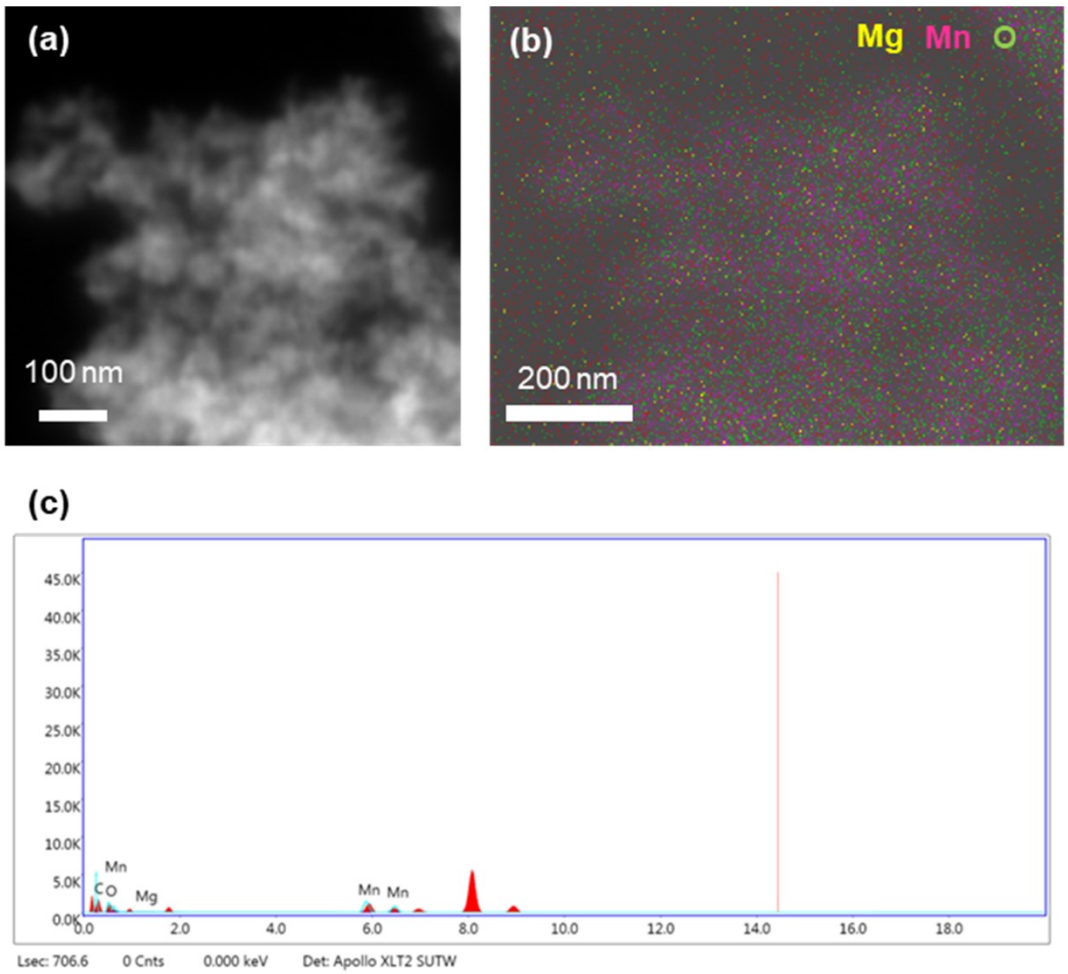

Figure S13. EDS results obtained from the HAADF-STEM.

(a) HAADF-STEM image of the Mg-doped MnO_2 particles. (b) overlapped EDS mapping of Mg, Mn and O elements. (c) EDS spectrum.

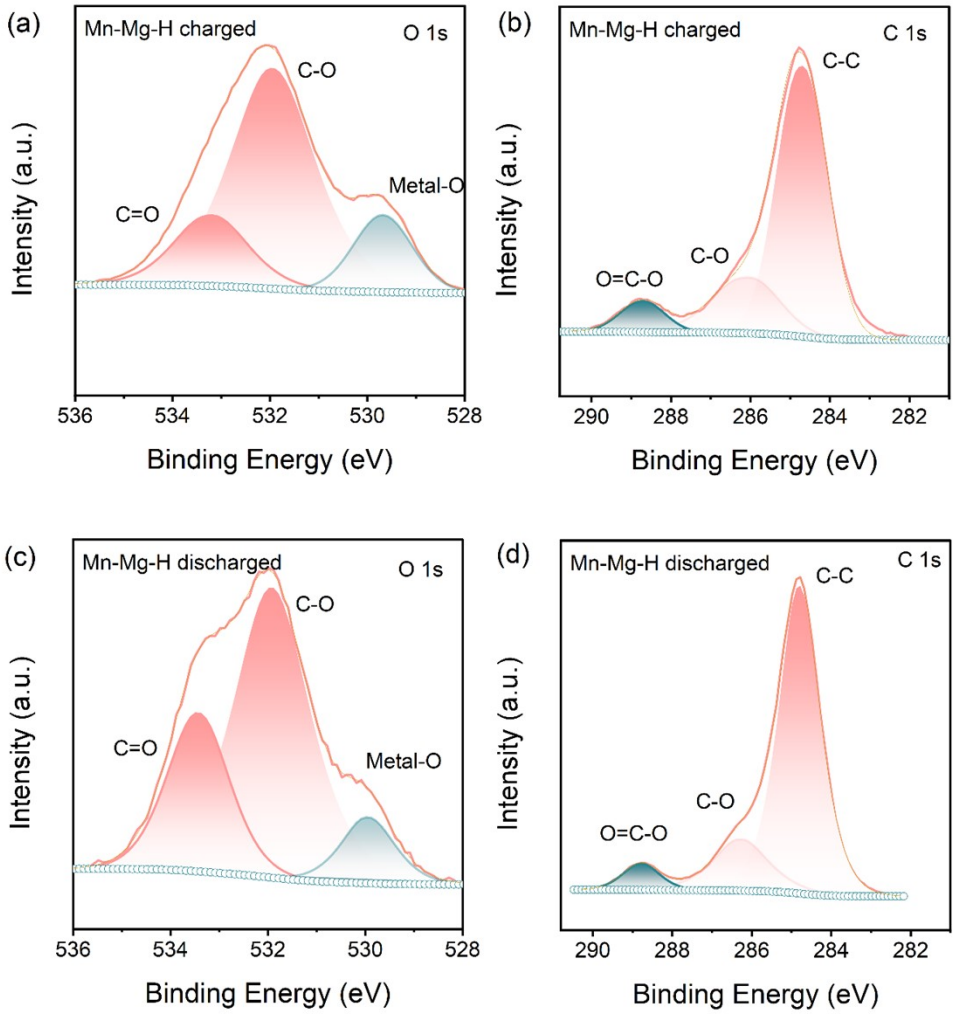

1

2 Figure S14. XPS spectra of discharged and recharged cathodes in Mn-Mg-H electrolytes.

3 (a) O 1s and (b) C 1s XPS spectra of the charged cathode. (c) O 1s and (d) C 1s XPS spectra of discharged cathode

4 The decreased intensity of Metal-O and increased intensity of C-O related species after discharge prove the reversible

5 decomposition of Mg-doped MnO_2.

Table S1. Smart Quant Results collected by the EDS of HAADF-STEM.

Element	Weight %	Atomic %	Net Error%
C K	46.83	72.13	0.67
O K	12.08	13.97	1.93
MgK	0.14	0.11	13.97
MnK	40.95	13.79	0.72
C K	46.83	72.13	0.67

Table S2. ICP-MS results of the Mg-doped MnO_2 charged products

Sample	Sample volume (mL)	Calibration volume/V_0 (mL)	Measurement concentration/ C_0 (mg/L)	Dilution factor/f	Dilutor/Sample concentration/C_1 (mg/L)	Sample concentration/ C_x (mg/L)	Stoichiometric ratio
Mg	1	1	0.3181	1	0.3181	3.18	0.015
Mg	1	1	0.3181	1	0.3181	3.23	0.015
Mg	1	1	0.3181	1	0.3181	3.21	0.015
Mn	1	10	4.5718	10	45.7178	457.18	0.985
Mn	1	10	4.6956	10	46.9559	469.56	0.985
Mn	1	10	4.6462	10	46.4617	464.62	0.985

Due to the large concentration difference between the Mn and Mg elements, the samples for Mn were diluted by a factor of 10 during the volumetric calibration (V_0) and measuring sessions (*dilute factor f*), respectively. In contrast, the Mg samples were maintained at primitive concentration. The relative stoichiometric ratios of the elements Mg and Mn were obtained from three separate tests on two sets of samples, and the conversion equations are shown in (1)-(4).

$$C_x(mg/L) = \frac{C_x(mg/L) * f * V_0(mL) * 10^{-3}}{m(g) * 10^{-3}} = \frac{C_1(mg/L) * V_0(mL) * 10^{-3}}{m(g) * 10^{-3}} \quad (1)$$

$$C_1(mg/L) = C_0(mg/L) * f \quad (2)$$

$$x(Mg) = \frac{\frac{C_x(mg/L)}{M(Mg)}}{\frac{C_x(mg/L)}{M(Mg)} + \frac{C_x(mg/L)}{M(Mn)}} \quad (3)$$

$$x(Mn) = 1 - x(Mg) \quad (4)$$

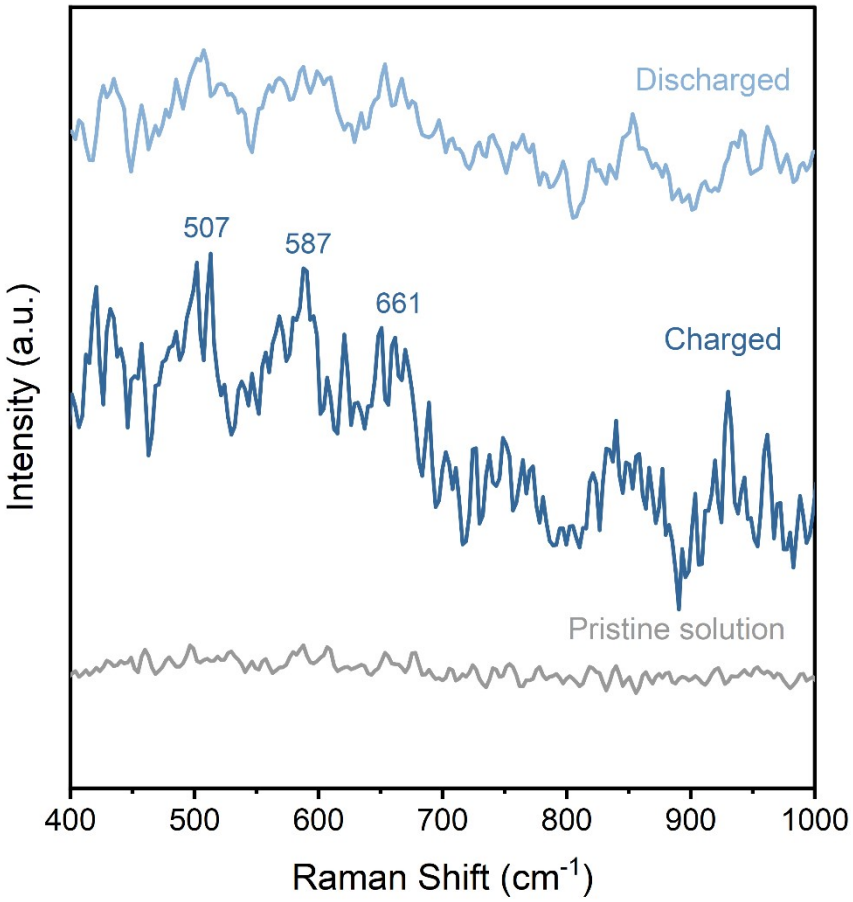

Figure S15. Raman spectra of the Mn-Mg-H electrolytes.

The appearance and weakening of the characteristic peaks demonstrate the reversible formation and decomposition of Mg-doped MnO_2 products in the electrolytes.

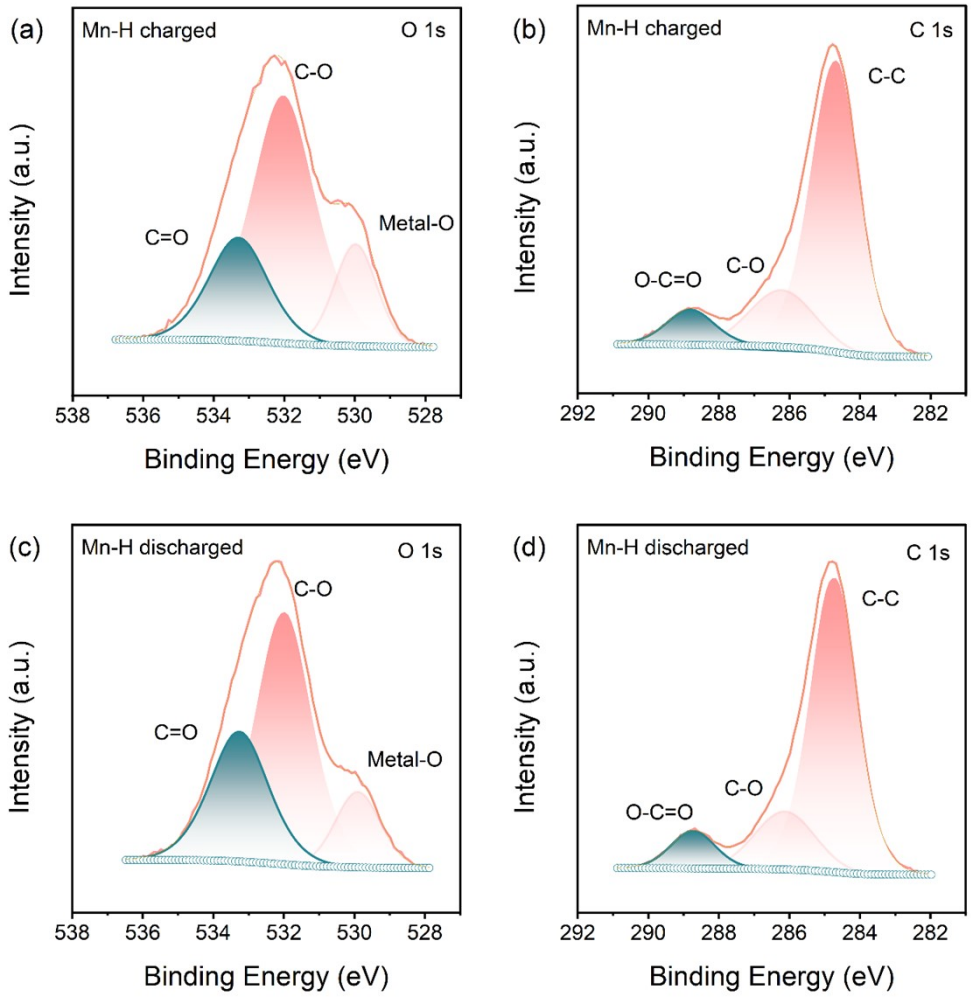

1

2 Figure S16. XPS spectra of discharged and recharged cathodes in Mn-H electrolytes.

3 (a) O 1s and (b) C 1s XPS spectra of the charged cathode. (c) O 1s and (d) C 1s XPS spectra of discharged cathode.

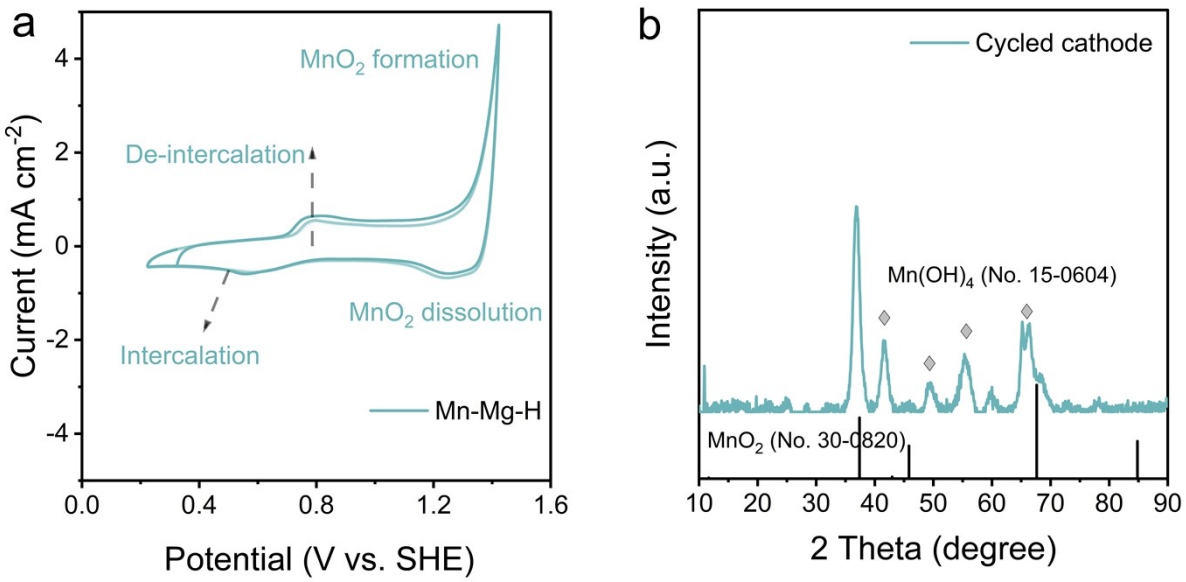

1

2 Figure S17. Characterization of the intercalation behavior occurring during cycling.

3 (a) Initial cycles of Cyclic voltammetry (CV) of cathode reaction in Mn-Mg-H electrolytes. (b) X-ray diffraction

4 (XRD) of the cycled cathode of Mn-Mg-H based Zn-Mn FBs.

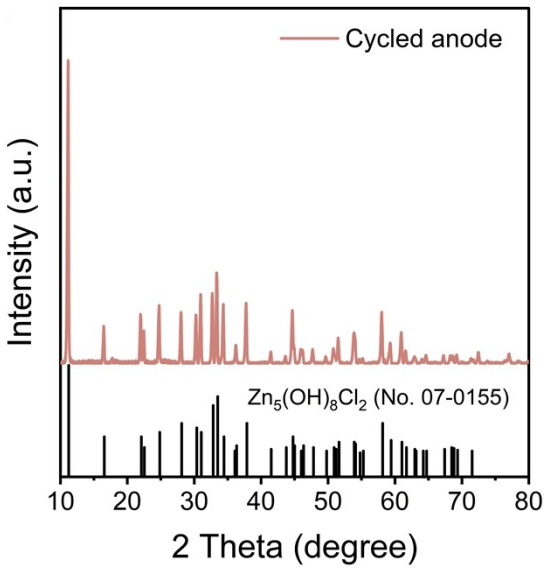

Figure S18. X-ray diffraction (XRD) of the cycled anode of Mn-Mg-H based Zn-Mn FBs

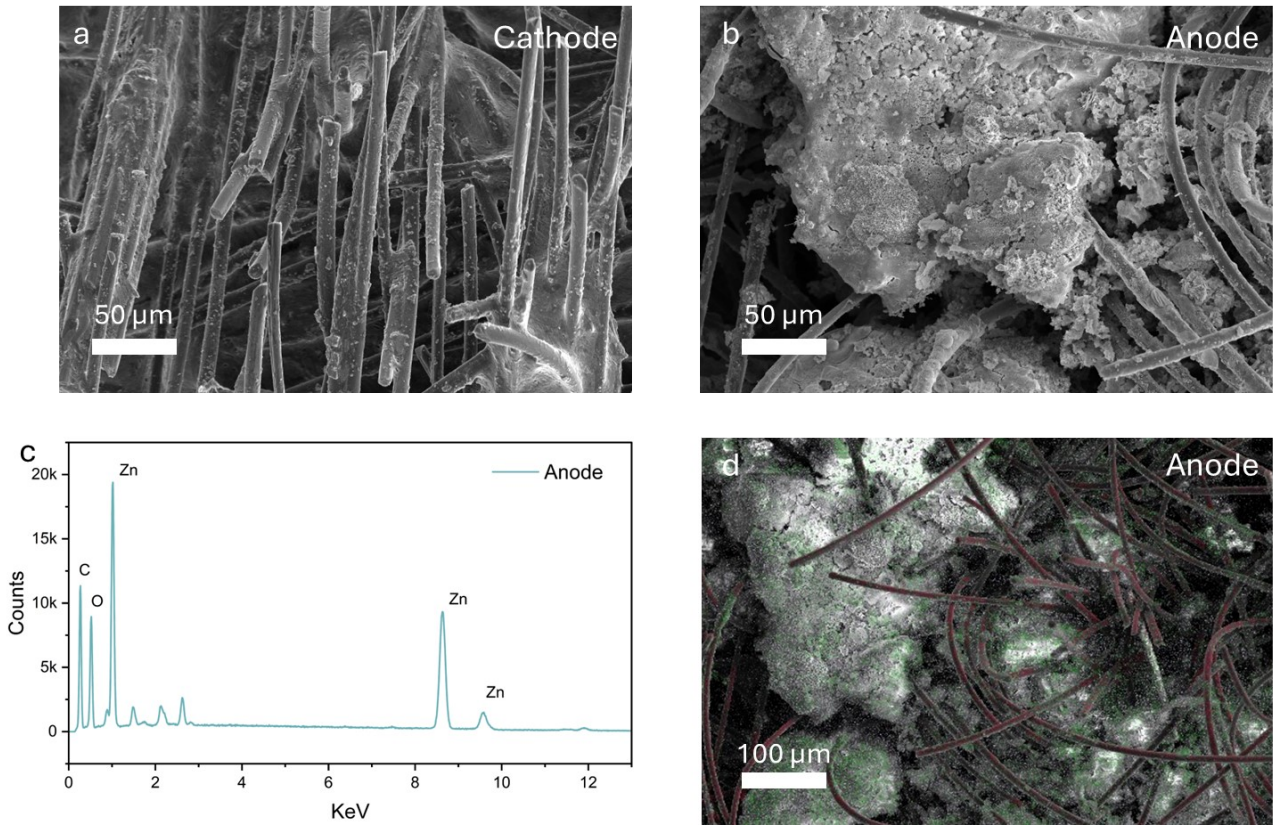

Figure S19. Characterization of the electrodes of the failed Zn-Mn FBs.

SEM image of the cycled (a) cathode and (b) anode of the Mn-Mg-H based Zn-Mn FBs. (c) Energy-dispersive X-ray spectroscopy (EDS) of the cycled anode. (d) Overlayed EDS mapping of the cycled anode.

1 Table S3. Smart quantitative results obtained from the Energy-dispersive X-ray spectroscopy (EDS)

Element	Weight (%)	Atomic (%)	Net Int.	K-ratio
C	41.8	65.6	305.5	0.1011
O	19.1	22.5	264.3	0.0320
Zn	35.1	10.1	728.8	0.2872
Cl	1	0.6	99.4	0.0076
Au	1.1	0.8	68.1	0.0039

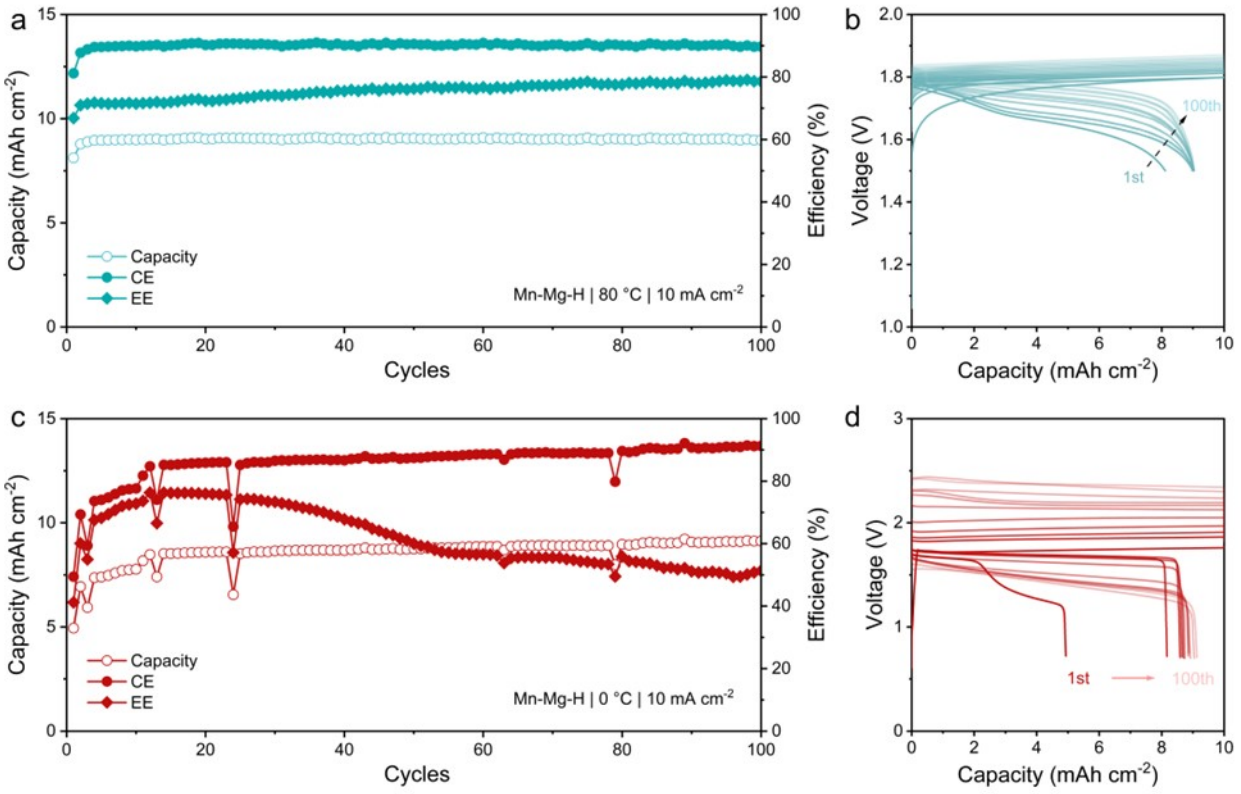

Figure S20. Cycling performance of the Zn-Mn FBs at different temperatures.

Cycling performance of the Zn-Mn FBs at (a) 80 ℃ and (b) the corresponding galvanostatic charge and discharge (GCD) profiles. (c) Cycling performance of Zn-Mn FBs at 0 ℃ and (d) the corresponding GCD profiles. All the batteries were charged to 10 mAh cm^{-2} at 10 mA cm^{-2}.

Table S4. Comparison of cycling performance of Zn-Mn FBs according to previous reports.

Article	Catholyte	Anolyte	Voltage (V)	Areal capacity (mAh cm^{-2})	Energy density (mWh cm^{-2})	Cycles
1[3]	1M $Mn(Ac)_2$ + 1M $Zn(Ac)_2$ + 2M KCl		1.5	7	10.5	400
2[4]	1M $Mn(Ac)_2$ + 1M $Zn(Ac)_2$ + 2M KCl + 0.1M KI		1.45	15	21.75	225
3[5]	1M $MnSO_4$+ 1M $ZnSO_4$		1.62	4	6.5	500
4[6]	1M $MnSO_4$, 0.09M $CoSO_4$, 0.06M $NiSO_4$ and 0.1M H_2SO_4		1.9	9.5	18.05	600
5[7]	1M Li_2SO_4 + 1M $ZnSO_4$		1.8	1.02	1.84	1000
6[8]	2.5M $NaMnO_4$ + 5M NaOH	0.2M $Na_2Zn(OH)_4$ + 5M NaOH.	1.9	1.75	3.33	1200
7[9]	0.5M EDTA-Mn + 3M NaCl	0.5M $ZnCl_2$ + 3M NaCl	1.35	1.67	2.25	400
8[10]	0.4 vol% MnO_2 in 2 M $ZnSO_4$ + 0.1 M $MnSO_4$	Zn pellets and Zn foil	1.35	4.21	5.68	100
9[11]	2M $MnSO_4$+1M KCl	2M $ZnSO_4$+1M KCl	1.85	8.3	15.36	100
10[12]	0.025 M $FeSO_4$ + 1 M $MnSO_4$ + 0.5 M H_2SO_4 + 1 M Na_2SO_4	1M $ZnSO_4$ + 1M NaAc + 1M HAc	1.91	10	19.1	200
11[13]	0.5M H_2SO_4 + 1M $MnSO_4$	2.4M KOH, and 0.1M $Zn(Ac)_2$	2.3	0.4	0.92	1500
12[14]	0.1M $MnSO_4$ + 2.5M H_2SO_4 with BiO catalyst	0.1M $[Zn(OH)_4]^{2-}$ + 4M NaOH	2.5	7	17.5	150
13[15]	0.2M $MnSO_4$ and 1M H_2SO_4	0.2M $ZnSO_4$ and 2M NaOH	2.2	1	2.2	100

Reference

1 H. Sun, *J. Phys. Chem. B*, 1998, **102**, 7338–7364.

2 M. P. Tosi, in *Solid State Physics*, eds. F. Seitz and D. Turnbull, Academic Press, 1964, vol. 16, pp. 1–120.

3 C. Xie, T. Li, C. Deng, Y. Song, H. Zhang and X. Li, *Energy Environ. Sci.*, 2020, **13**, 135–143.

4 J. Lei, Y. Yao, Z. Wang and Y.-C. Lu, *Energy & Environmental Science*, 2021, **14**, 4418–4426.

5 G. Li, W. Chen, H. Zhang, Y. Gong, F. Shi, J. Wang, R. Zhang, G. Chen, Y. Jin, T. Wu, Z. Tang and Y. Cui, *Adv. Energy Mater.*, 2020, **10**, 1902085.

6 M. Chuai, J. Yang, M. Wang, Y. Yuan, Z. Liu, Y. Xu, Y. Yin, J. Sun, X. Zheng, N. Chen and W. Chen, *eScience*, 2021, **1**, 178–185.

7 N. Liu, M. K, J. Pan, Y. Hu, Y. Sun and X. Liu, *J. Electrochem. Soc.*, 2020, **167**, 040517.

8 W. Xiang, M. Yang, M. Ding, X. Chen, J. Liu, G. Zhou, C. Jia and G. I. N. Waterhouse, *Energy Storage Materials*, 2023, **61**, 102894.

9 X. Yu, Y. Song and A. Tang, *Journal of Power Sources*, 2021, **507**, 230295.

10 T. M. Narayanan, Y. G. Zhu, E. Gençer, G. McKinley and Y. Shao-Horn, *Joule*, 2021, **5**, 2934–2954.

11 R. pandiyan Naresh, K. Mariyappan, D. Dixon, M. Ulaganathan and P. Ragupathy, *Batteries & Supercaps*, 2021, **4**, 1464–1472.

12 Q. Wang, W. Zhou, Y. Zhang, H. Jin, X. Li, T. Zhang, B. Wang, R. Zhao, J. Zhang, W. Li, Y. Qiao, C. Jia, D. Zhao and D. Chao, *National Science Review*, 2024, **11**, nwae230.

13 C. Liu, X. Chi, Q. Han and Y. Liu, *Advanced Energy Materials*, 2020, **10**, 1903589.

14 M. Kim, S. Lee, J. Choi, J. Park, J.-W. Park and M. Park, *Energy Storage Materials*, 2023, **55**, 698–707.

15 B. Kim, Y. S. Kim, D. Dulyawat and C.-H. Chung, *Journal of Energy Storage*, 2023, **72**, 108337.